



Investigation on cutting mechanism and micro-damage evolution in orthogonal cutting of T300/USN20000-7901 unidirectional laminates

Shengping Zhang¹ · Junshan Hu^{1,2} · Shanyong Xuan² · Jiali Yu² · Ruihao Kang¹ · Wei Tian¹

Received: 26 September 2022 / Accepted: 7 April 2023 / Published online: 19 April 2023
© The Author(s), under exclusive licence to Springer-Verlag London Ltd., part of Springer Nature 2023

Abstract

This paper investigated the cutting behaviors and chip formation in machining of carbon fiber reinforced polymer (CFRP) composites. The single cutting edge and unidirectional (UD) laminates of six different fiber orientations from 0° to 150° with an interval of 30° were employed in the orthogonal cutting test. The effects of fiber cutting angle, cutting speed and cutting depth on cutting mechanism and micro-damage evolution were estimated. Cutting force and thrust force obtained by dynamometer were used to evaluate the interaction between the tool and the workpiece. Subsurface damage was assessed by damage depth and failure mode of microstructure such as fiber and matrix. The machined surface roughness was used to characterize the machined surface quality. The results indicated that the average cutting force at $\theta > 90^\circ$ was 7.58 times higher than that at $\theta < 90^\circ$ and large deformed fibers below the machined surface existed elasticity recovery in the former case. The cutting speed and cutting depth had the most significant effects on the cutting force at $\theta = 90^\circ$ where the fiber bending deformation and fiber kinking keep cutting force at a high level. The micromorphology of machined surface and subsurface revealed four typical cutting mechanisms, namely, interface-debonding, fracture-sliding, shearing-fracture, and bending-fracture in the range of $\theta = 0 \sim 180^\circ$. The variation trend of surface roughness with cutting parameters at $\theta > 90^\circ$ is obvious and in consistent with that of cutting force. The most efficient factor on the roughness is found to be the fiber cutting angle accounting for 98.60%, followed by the cutting depth (0.55%) and cutting speed (0.25%). The interaction between the factors is not significant according to the results of ANOVA.

Keywords CFRP composites · Orthogonal cutting · Cutting mechanism · Chip formation · Surface morphology

1 Introduction

Carbon fiber reinforced polymer (CFRP) have been gradually applied to critical structures of aircrafts to reduce the structural weight by 20% to 40% and enhance overall performance due to their excellent properties such as light weight, high strength and good fatigue resistance over conventional

materials [1, 2]. CFRPs are often formed directly into monolithic component in order to reduce the number of assembly connectors and improve structural integrity by “near net shape” method because of their flexible designability [3]. Nevertheless, it is inevitable to reprocess CFRP components through various machining methods like drilling and milling to obtain assembly hole and desired structure feature, respectively [4]. However, CFRPs are typically difficult to machining and are liable to form burrs, tear [5, 6] and delamination [7] due to their anisotropy and heterogeneity, which seriously weakens the assembly reliability and stability of service performance of the components [8]. In addition, the strict damage tolerance brings tough challenges to the machining of CFRP.

Actually, extensive and in-depth research on the damage of CFRP drilling and milling has been carried out. As the most crucial damage type [9], the degree of delamination determines the mechanical properties of composites directly. Studies reveal that

✉ Junshan Hu
hujunshan@nuaa.edu.cn

✉ Wei Tian
tw_nj@nuaa.edu.cn

¹ College of Mechanical and Electrical Engineering, Nanjing University of Aeronautics and Astronautics, Nanjing 210016, China

² State-Operated Wuhu Machinery Factory, No. 99, Nanyang Road, Wuhu 241007, China

the drilling axial force and milling force are the primary cause of delamination in CFRP drilling and milling, respectively [10, 11]. In terms of machining parameter, the rotational speed and feed speed are the most concerned contributing factors due to their remarkable effects on the cutting force. The drilling axial force increases sharply with rise of feed speed [12, 13], accompanied by serious delamination at the drilling exit [14]. While the higher rotational speed can reduce axial force and obtain good surface quality. Furthermore, the feed speed has more obvious effect on the axial force than spindle speed [15]. At exit of hole, burrs usually appear in areas where the fiber cutting angle is obtuse and tearing damage is concentrated in right angle area. While there are no defects in acute angle region [16]. The milling force is also strongly related to milling parameters. It decreases with the growth of rotational speed while increases with axial depth of cut, radial depth of cut and feed rate [17, 18], of which the depth of cut has the greatest impact on the milling force. Milling defects such as edge breakage, burrs, tearing, and delamination are more serious when fiber cutting angle is greater than 90° , especially in the ranges from 90° to 135° [19, 20].

Essentially, the drilling or milling of CFRP on the macro level is the removal process of fiber and matrix at the micro level. The defects in drilling or milling can be unified as different forms and degrees of micro-damage such as fiber breakage, matrix cracking and interface debonding. In order to study damage mechanism of microstructure such as fiber, matrix and interface between them, Koplev [21] proposed a method of cutting CFRP with a single cutting edge, namely orthogonal cutting experiment. It is concluded that the cutting mechanism of CFRP was related to the fiber direction, and the chip removal was the result of brittle fracture of materials. Since then, orthogonal cutting experiment was regarded as a classical method to study microscopic damage during machining of CFRP [22, 23]. Wang et al. [24] analyzed the effect of fiber orientation, rake angle and depth of cut on cutting force, surface roughness and subsurface structure morphology. It revealed that 90° was a critical angle, beyond which the cutting mechanism becomes more complicated and the subsurface damage caused by fiber bending and fiber-matrix debonding would be more severe. Jahromi [25] found that the length of the broken fibers increased with increase of fiber orientation. Moreover, the cracks depth was limited within $15\ \mu\text{m}$ when fiber orientation is between 0° and 45° , while the crack propagation depth can reach $225\ \mu\text{m}$ owing to interface debonding in the situations of $90^\circ < \theta < 135^\circ$ [26]. Bhatnagar et al. [27] proposed a predictive model considering frictional conditions and tool geometric parameters to forecast the chip formation and cutting force based on the relationship between cutting force and fiber orientation angle in orthogonal cutting test. Agarwal et al. [28] studied the chip formation, cutting force and strain distribution obtained by digital image correlation (DIC) technology. It is realized that chip formation was determined by cutting depth and fiber orientation. An et al. [29] analyzed fracture mechanism of CFRP and machined surface

morphology under different fiber orientation angle. Overall, the investigation for the machining responses of composites such as the cutting force, crack growth and machined surface quality offered the essential knowledge to understand the interaction between composite and cutting tool.

Apart from the above experimental investigation, numerical simulation models to characterize the dynamic process of chip formation and predict cutting force under different cutting conditions had been developed because of high costs for machining of composite materials. Rao et al. used a two-phase micro-mechanical model [30] and a three-dimensional macro-mechanical model successively [31] to predict the cutting force under different fiber orientations within certain range, cutting depth and rake angle of the tool during machining of UD-CFRP. It revealed that the cutting force increased with fiber orientation and cutting depth but was less affected by rake angle of the tool. Hassouna [32] demonstrated that the maximum cutting force was observed at fiber orientation angle of 90° both in macro-mechanical model and in micro-mechanical model. The high fracture energy caused large material deformation, resulting in severe subsurface. Yan et al. [33] calculated material fracture energy (fiber damage, matrix damage and fiber-matrix interfacial debonding), plastic dissipation energy of matrix and frictional dissipation energy from a three-dimensional thermo-mechanical finite element (FE) model. The energy for various fiber cutting angle, depth of cut and rake angle were analyzed to quantify the different energy dissipation mechanisms and dominant damage mode. In addition, most FE simulation improved simulation accuracy by optimizing material properties including constitutive relationship, damage evolution rule and element failure criteria [34, 35], and modeling settings including modeling method such as equivalent homogeneous model [36] and multi-scale model [37], and FE preprocessing setting such as the contact property and meshing [38].

The efforts mentioned above in investigating the cutting responses of composites by experimental and numerical methods enrich the research content of high efficiency cutting technology of composites and provide a profound understanding for anisotropy and heterogeneity of composite materials. To the authors' best knowledge, few studies have paid attention to the difference of the influence of cutting parameters on cutting response at different fiber cutting angles in orthogonal cutting test. In addition, the failure modes and damage evolution of microstructure with the change of cutting conditions are also unclear. As a result, the selection and adjustment of composite cutting parameters lack theoretical basis and rely more on personal experience. It is difficult to ensure the consistency and stability of composite cutting quality. These facts have led the authors to focus on current investigation, which involves analysis of cutting response and removal mechanism of microstructure like fiber and matrix in machining of CFRP. Special attention

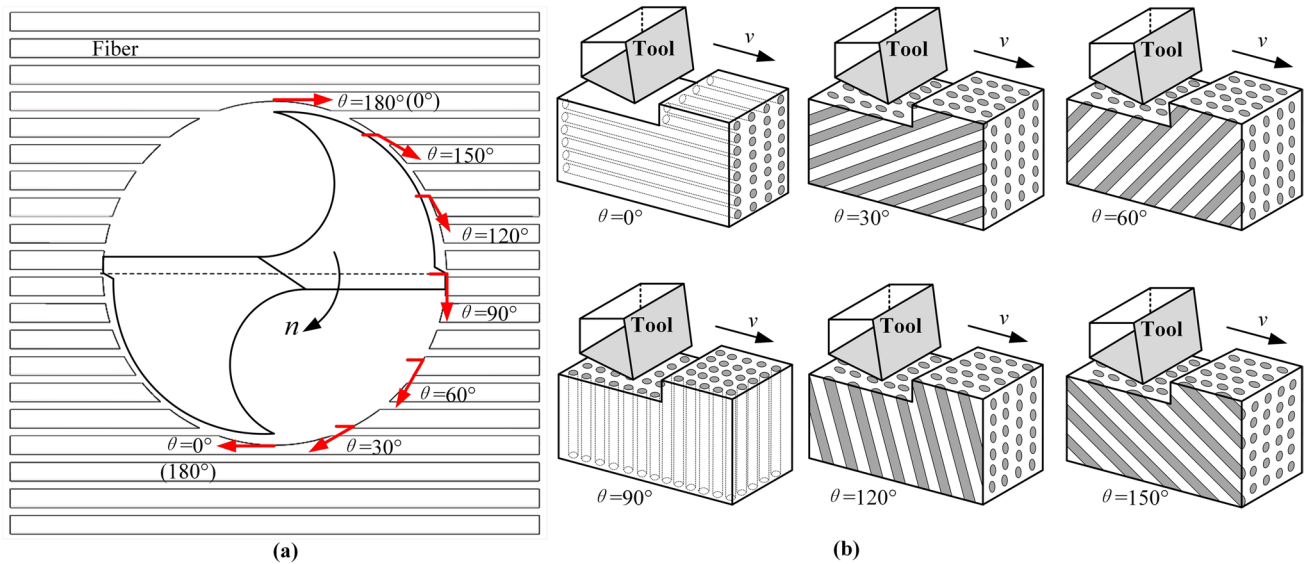


Fig. 1 The schematic diagram of drilling process: (a) the top view of composite drilling and (b) orthogonal cutting model

was paid to the fiber cutting angle, cutting speed and cutting depth. The cutting force, thrust force, machined surface morphology, microstructure damage and chip shape were used to characterize cutting behaviors of UD laminates in orthogonal cutting test. It is hoped that these findings in this paper would provide guidance for the machining of composites.

2 Experimental procedure

2.1 Problem configuration

The top view of composite drilling is illustrated in Fig. 1a. With the rotation of the drill bit, fibers are successively cut off by the tool edge in a direction that is parallel, at a blunt angle, perpendicular and at an acute angle to the fibers. The fiber cutting angle (FCA, θ) in drilling is defined by the angle between the direction of fiber bundles and tangent direction of cutting edge. The FCA changes rapidly and periodically, meanwhile the drill is in semi-sealing situation during drilling. Therefore, not only it is difficult to analyze the damage discrepancy of composite drilling along the circumferential direction from the micro level, but also the effect of rotational speed and feed speed on the deformation and removal of material are hard to evaluate. So the differential element method is applied to establish the connection between

micro-mechanical model and macro-mechanical model. The main cutting edges in drilling or milling are divided into small micro cutting elements so that the complex cutting process of main cutting edge can be simplified as the cutting process of single cutting edge. Orthogonal cutting model is shown in Fig. 1b. The fiber cutting angle in orthogonal cutting model represents the angle between fiber orientation and cutting speed. The cutting speed and cutting depth in the orthogonal cutting model can be calculated from drilling parameters such as the rotational speed, feed speed and tool diameter by the differential element method [39]. Hence the fiber cutting angle, cutting speed and cutting depth are key factors of orthogonal cutting model in the present research.

2.2 Materials and specimen preparation

The UD-CFRP laminates were manufactured by Guangwei Composites Co., Ltd., China using vacuum bag molding process. Unsaturated polyester resin 7901 was used as matrix and unidirectional standard modulus carbon fiber prepreg USN 20,000 was used as reinforcement. The mechanical properties of UD laminates were presented in Table 1. The cured laminates with a total thickness of 3 mm were cut into 90 mm × 10 mm specimens with six

Table 1 The mechanical properties of UD laminates

Mechanical properties	ρ (g/cm ³)	T_g (°C)	E_1 (Gpa)	E_2 (Gpa)	G_{12} (Gpa)	ν_{12}	X_t (Mpa)	X_c (Mpa)	Y_t (Mpa)	Y_c (Mpa)	S_{12} (MPa)
Values	1.6	110	120	8	4.5	0.25	1800	1200	55	200	100

Table 2 Tool geometry and cutting conditions

Category	Parameters	Values
Tool geometry	Cutting edge width w (mm)	9
	Cutting edge radius r (mm)	0.01
	Rake angle α (°)	15
	Clearance angle γ (°)	25
Cutting conditions	Fiber cutting angle θ (°)	0, 30, 60, 90, 120, 150
	Cutting depth h (mm)	0.02, 0.04, 0.06
	Cutting speed v (mm/s)	4, 7, 10

types of fiber orientations, namely 0° , 30° , 60° , 90° , 120° and 150° as presented in Fig. 1b. The cemented carbide cutting tool used in the experiment was custom-made by Mapal China Ltd. The tool geometry parameters were listed in the Table 2.

2.3 Orthogonal cutting test

The experimental setups of orthogonal cutting test on UD-CFRP were presented in Fig. 2a. The cutting tool was installed on the spindle of CNC drilling machine (XK7124,

Zhongjie CNC Machine Tool Co., LTD, China). The UD-CFRP specimen was laterally fixed by the fixture. The details of the special fixture designed for the small specimen were shown in the three-dimensional cutaway view in Fig. 2b. The special fixture is composed of six parts, namely, strip-type clapboard, positioning block, cushion block, L-shaped left clamp plate, L-shaped right clamp plate and their pedestal. At first, the pedestal of fixture was fastened on the Kistler 9129AA dynamometer. Then the L-shaped left clamp plate was connected to the pedestal. After adjusting the cushion block to the center of the left clamp plate and keeping the holes of both parts coaxial, the L-shaped right clamp plate was bolted together with the cushion block and the left clamp plate. The positioning block was installed at one end of the cushion block. The UD laminate was placed on the cushion block with the positioning block as the reference. The bolts on the right clamp plate were rotated to press the strip-type clapboard so that the UD laminate was clamped on the vertical plane. The cutting edge was adjusted to be parallel to the thickness direction of the UD laminate.

The simplified schematic diagram of orthogonal cutting test was illustrated in Fig. 2c. The single cutting edge removed the material with a certain cutting depth (h) and cutting speed (v) along the horizontal direction. The cutting parameters selected in the test were listed in the Table 2.

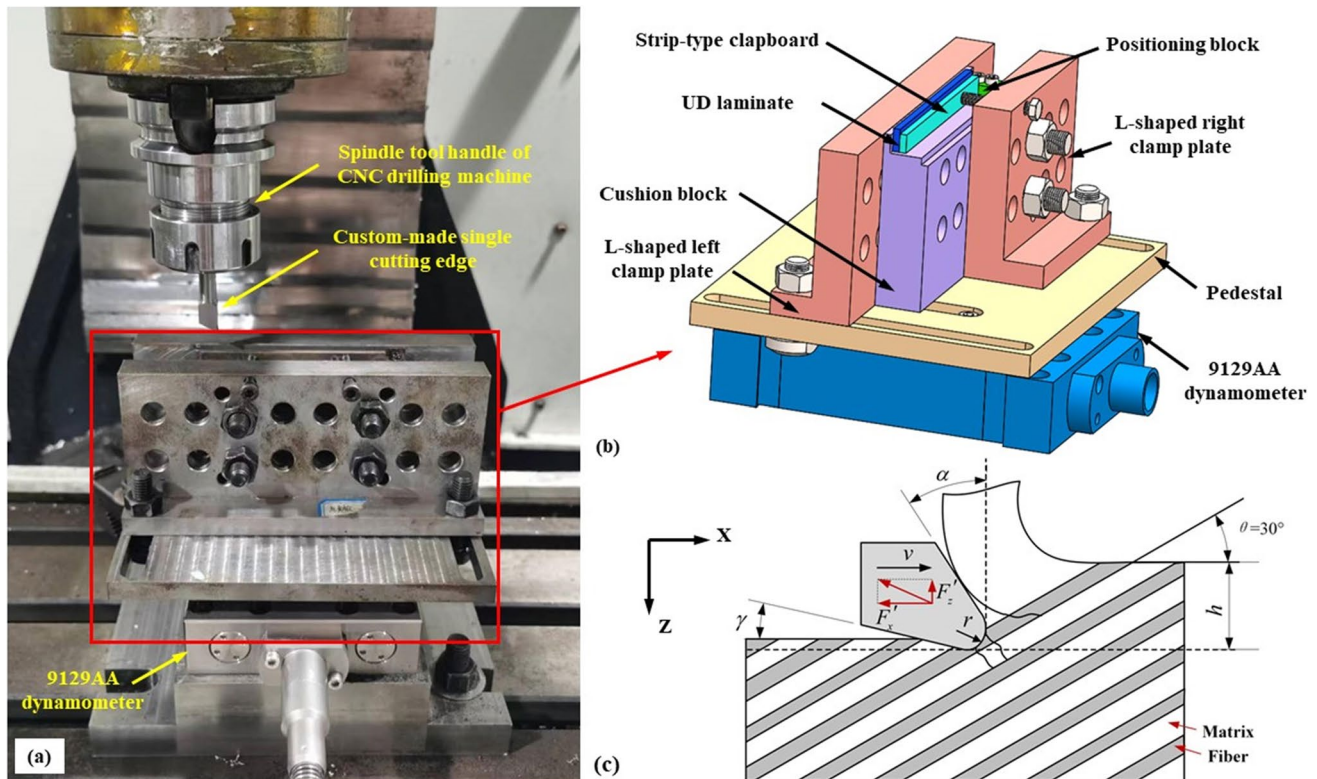
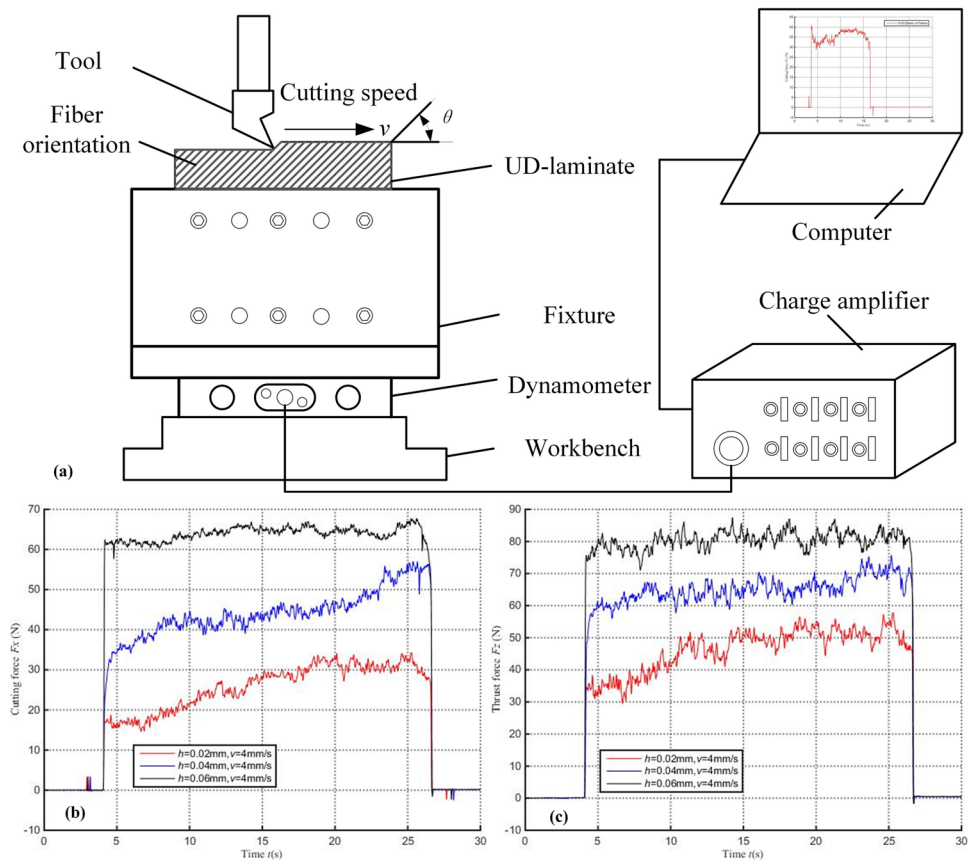


Fig. 2 Orthogonal cutting test: (a) the orthogonal cutting experimental platform; (b) special fixture designed for the small composite specimen; (c) the simplified schematic diagram of orthogonal cutting

Fig. 3 The diagram of: (a) Acquisition system of force signals; (b) The signals of cutting force F_x in X direction and (c) thrust force F_z in Z direction acquired in real time after low-pass filtering



During the test, the reaction force exerted by the CFRP specimen on the cutting tool was decomposed into two components, namely the cutting force (F'_x) and the thrust force (F'_z). The Kistler 9129AA dynamometer was connected with charge amplifier and computer to collect cutting force signal (F_x) in X direction and thrust force signal (F_z) in Z direction. The sampling frequency of force signals was set to be 10 kHz. Acquisition system of force signals is shown in Fig. 3a. The signals of cutting force (F_x) in X direction and thrust force (F_z) in Z direction acquired in real time after low-pass filtering are shown in Fig. 3b and c. For each kind

of cutting condition, the tests are repeated three times and the average of them was the final result. All the cutting tests were conducted under room temperature and dry condition.

After the test, UD-CFRP specimens were cleaned firstly so that the machined surface morphology can be inspected clearly by digital ultra-depth of field microscope (RH-2000, HIROX, China). Then the machined surface roughness was measured precisely by roughness meter (178–560-11DC/SJ-210, Mitutoyo, Japan). In order to observe subsurface damage, the specimens were cut into small cuboids of 1 mm × 1 mm × 3 mm, cleaned by

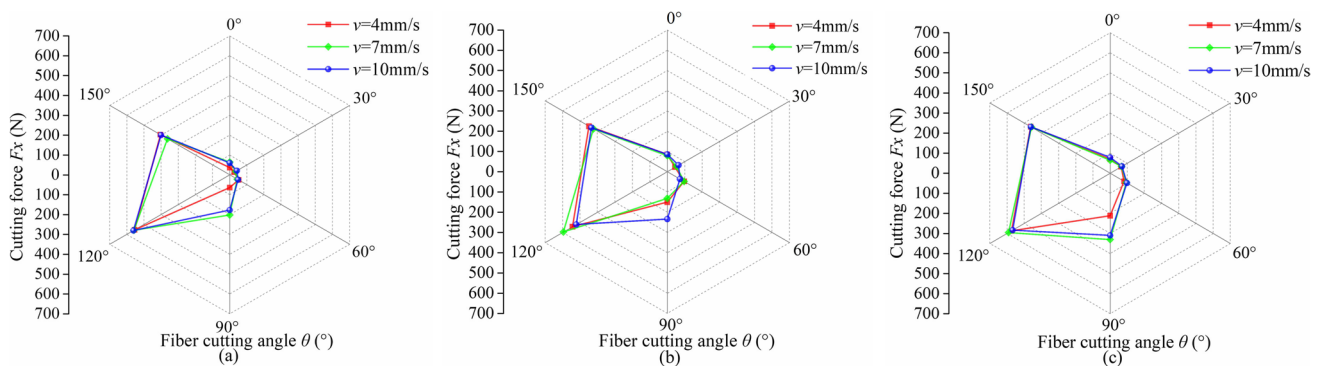


Fig. 4 The radar maps of cutting force varying with fiber cutting angle under different cutting speeds and cutting depths: (a) $h=0.02$ mm; (b) $h=0.04$ mm; (c) $h=0.06$ mm

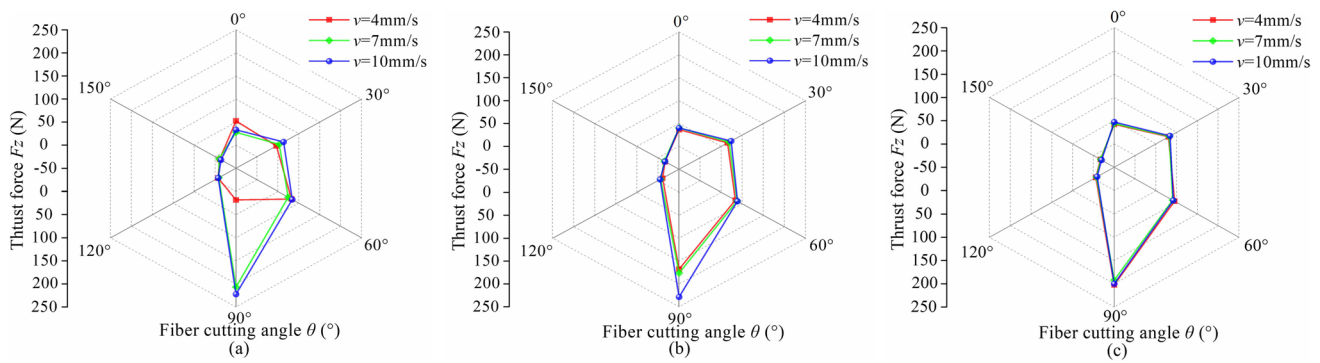


Fig. 5 The radar maps of thrust force varying with fiber cutting angle under different cutting speeds and cutting depths: (a) $h=0.02$ mm; (b) $h=0.04$ mm; (c) $h=0.06$ mm

ultrasonic cleaner and polished after cold mosaic treatment until subsurface damage can be seen clearly. The specific grinding and polishing process are as follows. The small cuboids samples after cold inlaying were ground with sandpaper of 800, 1200, 2000, 3000 and 5000 mesh successively. The grinding direction of the sample under each mesh number of sandpaper should be consistent to ensure the removal of the previous wear marks. After being ground, the samples were polished with a diamond spray polishing agent with a particle size of $1.5\ \mu\text{m}$ and polishing cloth until the subsurface of the samples were smooth without polishing marks. After being polished, the samples were cleaned by ultrasonic wave, and the subsurface damages were observed by microscope.

3 Results and discussions

3.1 Influence of the fiber cutting angle on the cutting force and thrust force

The radar maps of cutting force varying with fiber cutting angle under different cutting speeds and cutting depths are presented in Fig. 4. It can be observed that all the values of

the cutting force are small from 0° to 60° , with a range of no more than 50 N. Then they climb up drastically to the peak values of around 550 N at $\theta=120^\circ$, followed by a decreasing trend. It's obvious that these curves get minimum value and maximum value at $\theta=30^\circ$ and $\theta=120^\circ$, respectively. In the cases of $\theta < 90^\circ$, the cutting forces fluctuate in a small range because the cutting edge of the tool is inserted into material directly to cut the fiber bundles. The fibers don't go through extrusion deformation. The energy required for material removal is low. In the cases of $\theta > 90^\circ$, the rake surface of the tool and fibers start in contact with each other firstly, then the fibers are squeezed laterally by the rake surface of the tool and bend to a point where they are chopped by the cutting edge or break after reaching the bending limit. The larger fiber deformation consumes more energy. The average cutting forces of $\theta > 90^\circ$ is 495.99 N. Compared with $\theta > 90^\circ$, the cutting forces of $\theta < 90^\circ$ are 65.45 N on average. Therefore, the average cutting force of $\theta > 90^\circ$ is 7.58 times higher than that of $\theta < 90^\circ$.

The radar maps of thrust force varying with fiber cutting angle under different cutting speeds and cutting depths are plotted in Fig. 5. It is evident that the thrust force increases as the fiber cutting angle is increased from $\theta=0^\circ$ to $\theta=90^\circ$ but it drops sharply and becomes negative in the situations

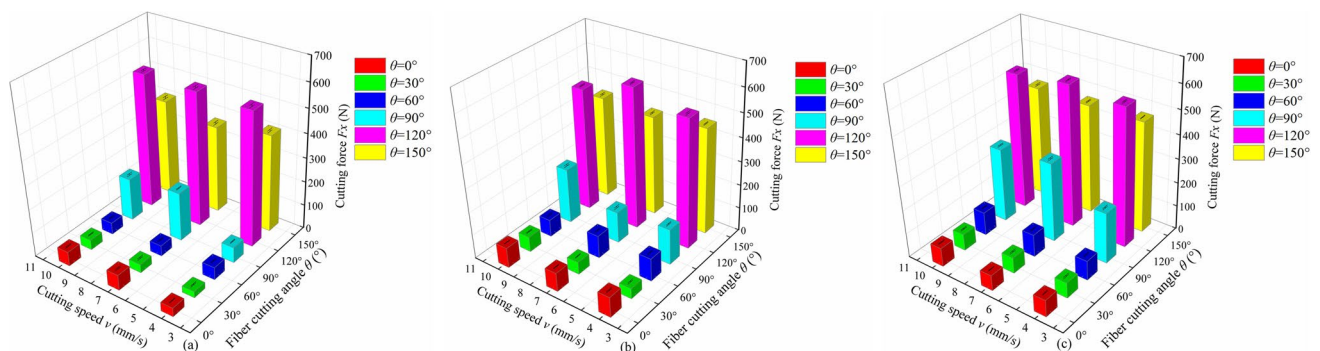
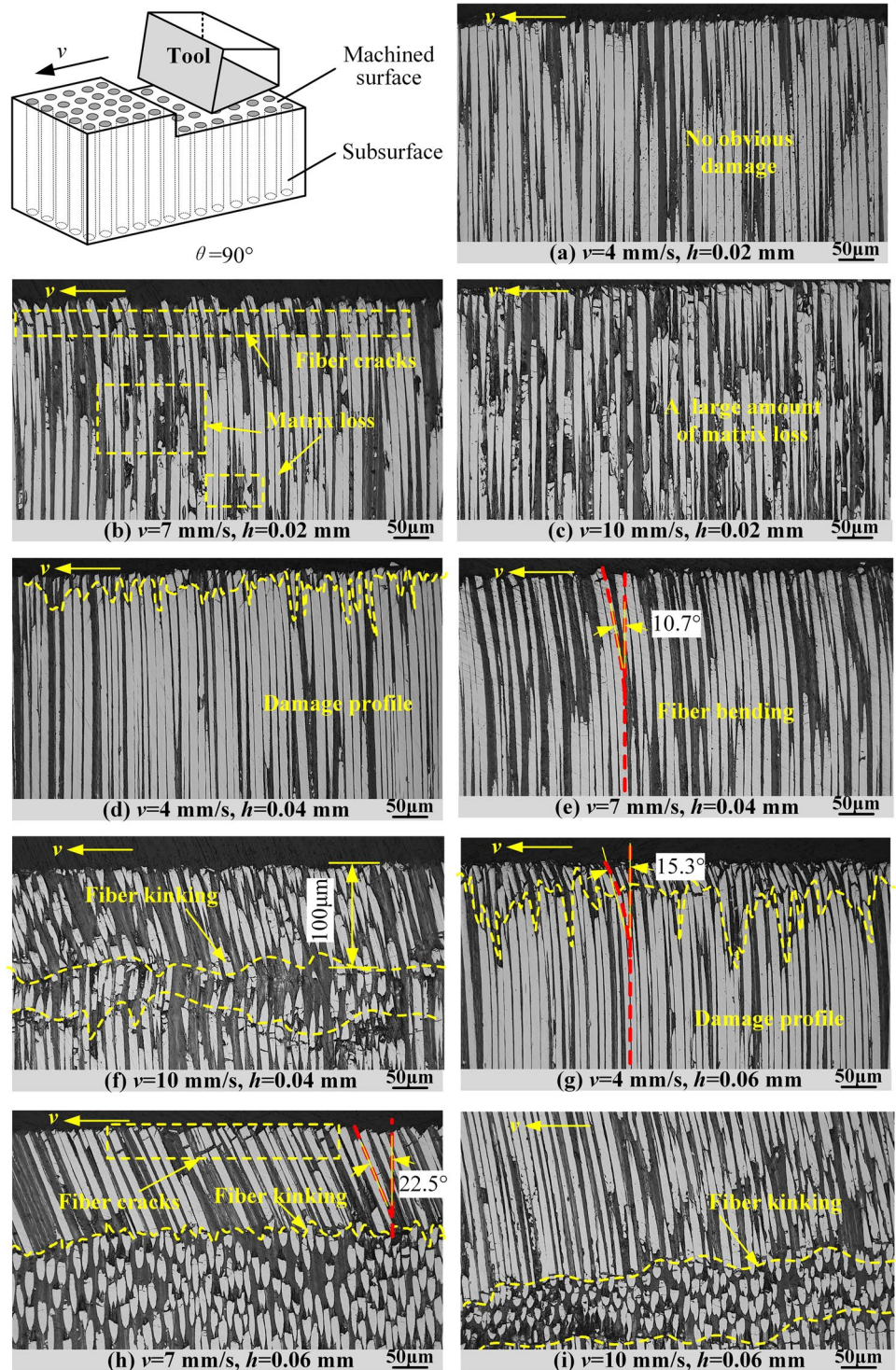


Fig. 6 The 3D bar diagrams of cutting force varying with the cutting speed at three different cutting depths: (a) $h=0.02$ mm; (b) $h=0.04$ mm; (c) $h=0.06$ mm

Fig. 7 The subsurface damages of UD-CFRP with $\theta=90^\circ$ in orthogonal cutting



of $\theta > 90^\circ$. Even though the thrust force switches to negative value, it still increases with fiber cutting angle in the opposite direction. It means that the force produced by cutting material with a tool in the vertical direction changes from downward push to upward pull. The phenomenon comes down to the effect of fiber elasticity recovery, which is in accordance with the result in Farid's research [40]. The

elasticity recovery of bended fibers exerts reaction force on the flank face of the tool, leading to reduction in cutting depth. Thus, real depth of cut is less than its nominal depth. Moreover, the bending fracture of the fibers above the machined surface produces tension along the fiber axis that causes the fibers pull-out. Therefore, not only the direction of the thrust force changes but also the value of the thrust

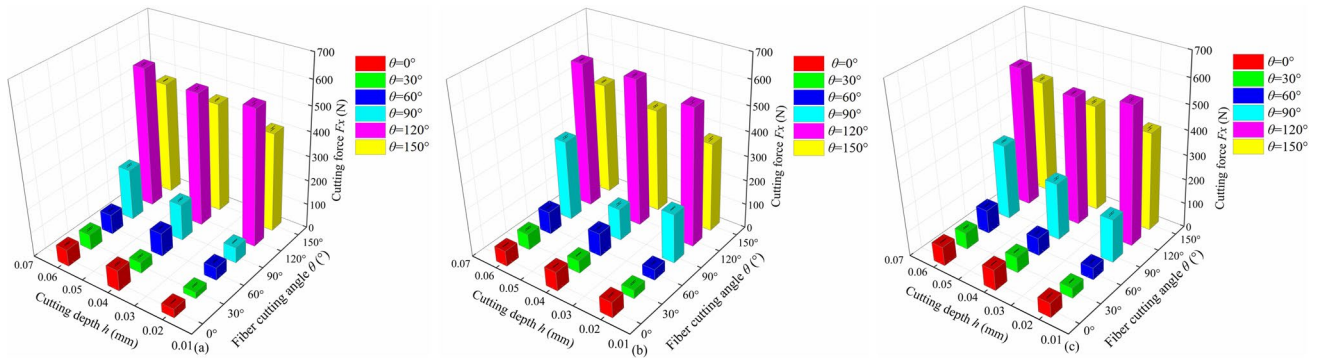


Fig. 8 The 3D bar diagrams of cutting force varying with cutting depth at three different cutting speeds:

force drops sharply to a low level within 25 N. Besides, it is worth noting that the thrust force under the condition of $v = 4$ mm/s in Fig. 5a doesn't reach maximum value at $\theta = 90^\circ$ like other curves. Instead, it falls to a value which is close to 20 N. That is because that the low cutting speed of 4 mm/s allows enough time for material deformation so that the elasticity recovery of the deformed fibers exerts opposite force on flank surface of the tool and further decrease the cutting depth which is already small ($h = 0.02$ mm), resulting in a significant decrease in thrust force.

3.2 Effect of the cutting speed and cutting depth on cutting force and damage evolution

It can be seen directly from Fig. 4 that the influence of cutting speed on cutting force is the most obvious at $\theta = 90^\circ$. In order to analyze the effect of cutting speed on cutting force deeply, the 3D bar diagrams of cutting force varying with the cutting speed at three different cutting depths are shown in Fig. 6. At

$\theta = 90^\circ$, the variation of cutting force in Fig. 6a and c have the same trend which increases first and then decreases with the growing cutting speed. Furthermore, both cutting forces at $v = 7$ mm/s and 10 mm/s are at a high level and they are 100 N to 150 N higher than those at $v = 4$ mm/s. While the variation of cutting force at $\theta = 90^\circ$ in Fig. 6b has an opposite tendency which declines first and then rises. The cutting force at $v = 10$ mm/s is about 100 N higher than cutting forces at $v = 4$ mm/s and 7 mm/s. These variations of cutting forces at $\theta = 90^\circ$ analyzed above can be reflected by the degree of subsurface damage of the UD laminates presented in Fig. 7.

In the cases of $h = 0.02$ mm and $v = 4$ mm/s, no obvious subsurface damage can be observed in Fig. 7a. There is no fiber deformation under the machined surface, and both fiber and matrix remain intact. Under the same cutting conditions, the cutting force is very small, only about 60 N in Fig. 6a. When the cutting speed is increased to 7 mm/s, fiber cracks and matrix loss can be seen in Fig. 7b. Fiber fracture is not neat and the height of broken fiber is different.

Fig. 9 At $\theta = 0^\circ$: (a) the subsurface damages of microstructure; (b) fiber deformation and stress state; (c) the chip morphologies; (d) the micro-morphologies of machined surface

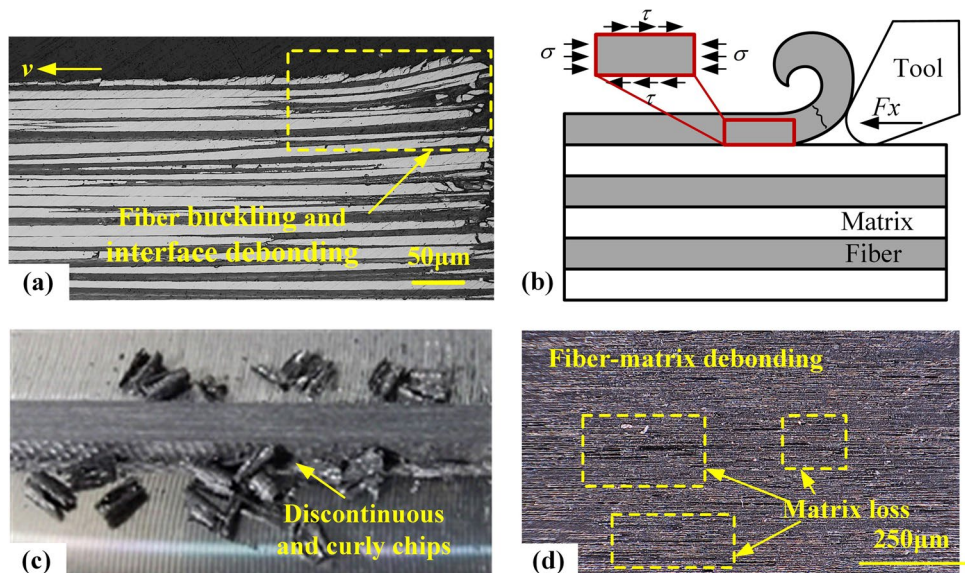
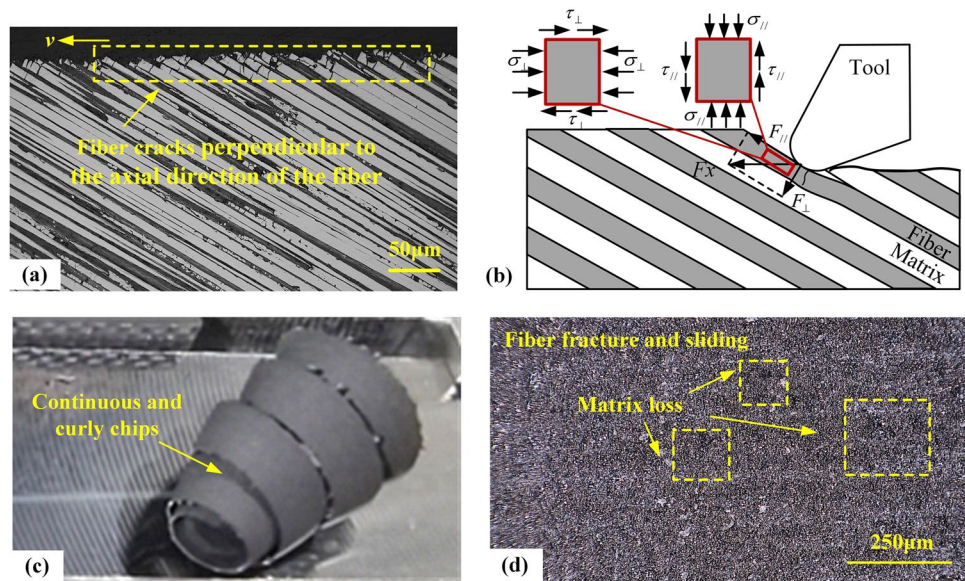


Fig. 10 At $\theta=30^\circ$: (a) the subsurface damages of microstructure; (b) fiber deformation and stress state; (c) the chip morphologies; (d) the micro-morphologies of machined surface



Obviously, the subsurface damage is more serious compared with former condition, and the cutting force of $\theta=90^\circ$ in Fig. 6a rises sharply from 60 N at $v=4$ mm/s to 200 N at $v=7$ mm/s. When the cutting speed continues to increase to 10 mm/s, the cutting force drops a little but it is still at a high level. Consistent with this variation, fiber cracking disappears, no fiber deformation can be observed except that a large amount of matrix loss occurs on the subsurface, as illustrated in Fig. 7c.

When the cutting depth is 0.06 mm, under the condition of $v=4$ mm/s in Fig. 7g, it shows a clear subsurface damage profile. There is no damage to the fibers and matrix below the damage profile while the angle of fiber bending is 15.3° . As the cutting speed increases to 7 mm/s in Fig. 7h, fiber kinking comes into being. Fiber kinking is a phenomenon of local shear deformation of the matrix along cutting direction and the fibers typically break at the edge of the kinking band. The fiber bundles above the kinking band are neatly tilted towards the cutting direction at an angle of 22.5° , accompanied by a few fiber cracks. The subsurface damage was apparently aggravated compared with Fig. 7g. It is seen in Fig. 7i that the kinking band moves down to a position where it is further away from the machined surface

due to the increase in the cutting speed. But the width of the kinking band decreases and the degree of fiber deformation between the kinking band and the machined surface is reduced. The degree of sub-surface damage alleviates in contrast to Fig. 7h. The degree of sub-surface damage is the same as variation trend of cutting force. The cutting force of $v=10$ mm/s is lower than that of $v=7$ mm/s at $\theta=90^\circ$ in Fig. 6c. Compared with the cutting force at $v=4$ mm/s, the cutting forces at $v=7$ mm/s and $v=10$ mm/s are at higher level.

When the cutting depth is 0.04 mm and the cutting speed is 4 mm/s in Fig. 7d, the damage profile is close to the machined surface and damage area is small. The fibers and matrix under the damage profile are not deformed and keep intact. As the cutting speed is increased to 7 mm/s in Fig. 7e, there are no fiber cracks and matrix loss on the subsurface, and the fibers are bent along the cutting direction with an inclination of 10.7° to the vertical direction. When the cutting speed is further increased to 10 mm/s in Fig. 7f, fiber kinking occurs at a distance of about $100 \mu\text{m}$ below the machined surface. The fibers above the kinking band are bent and break, presenting an elliptic-granule shape. Fiber cracking and matrix crushing can be seen. It is obvious in Fig. 6b that the cutting force of

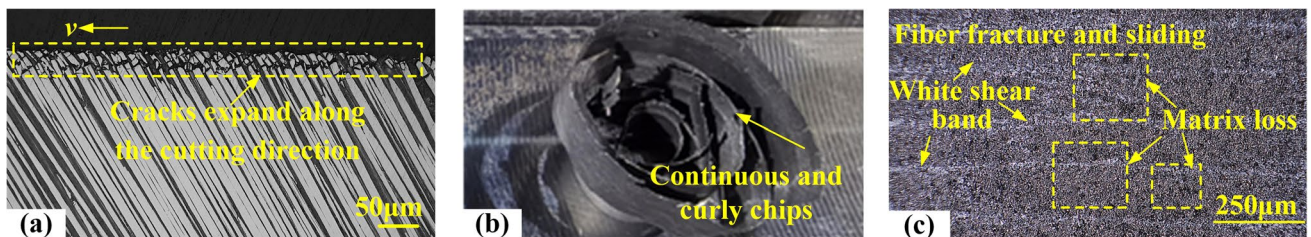
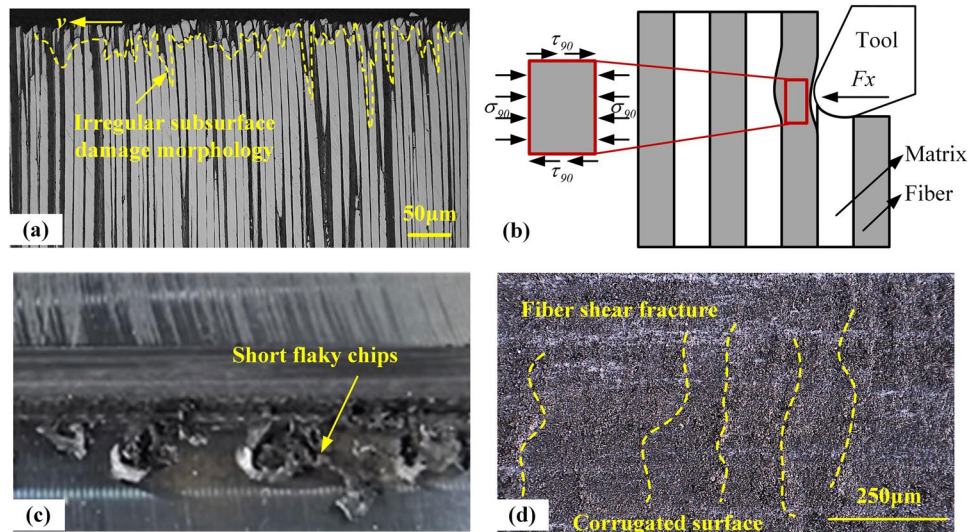


Fig. 11 At $\theta=60^\circ$: (a) the subsurface damages of microstructure; (b) the chip morphologies; (c) the micro-morphologies of machined surface

Fig. 12 At $\theta=90^\circ$: (a) the subsurface damages of micro-structure; (b) fiber deformation and stress state; (c) the chip morphologies; (d) the micro-morphologies of machined surface



$\theta=90^\circ$ at $v=10$ mm/s rises dramatically to around 240 N from a relatively low level of 130 N at $v=7$ mm/s. According to the above analysis of damage evolution, it can be concluded that low cutting speed and small cutting depth are beneficial to reduce subsurface damage at $\theta=90^\circ$.

Apart from the cutting speed, the cutting depth also affects the cutting force of UD laminates. The 3D bar diagrams of cutting force varying with cutting depth at

three different cutting speeds are presented in Fig. 8. It's clear that the cutting forces at $\theta=90^\circ$ fluctuate within a wide range with the increase of cutting depth. In particular, at $v=4$ mm/s in Fig. 8a and $v=10$ mm/s in Fig. 8c, the cutting force gradually increases with the cutting depth, sharing the same trend at $\theta=90^\circ$. The variation trend of cutting force is in accordance with degree of sub-surface damage. With the increase of cutting depth,

Fig. 13 At $\theta=120^\circ$: (a) the subsurface damages of micro-structure; (a-i) local enlarged detail at i in Fig. 13a; (b) fiber deformation and stress state; (c) the chip morphologies; (d) the micro-morphologies of machined surface

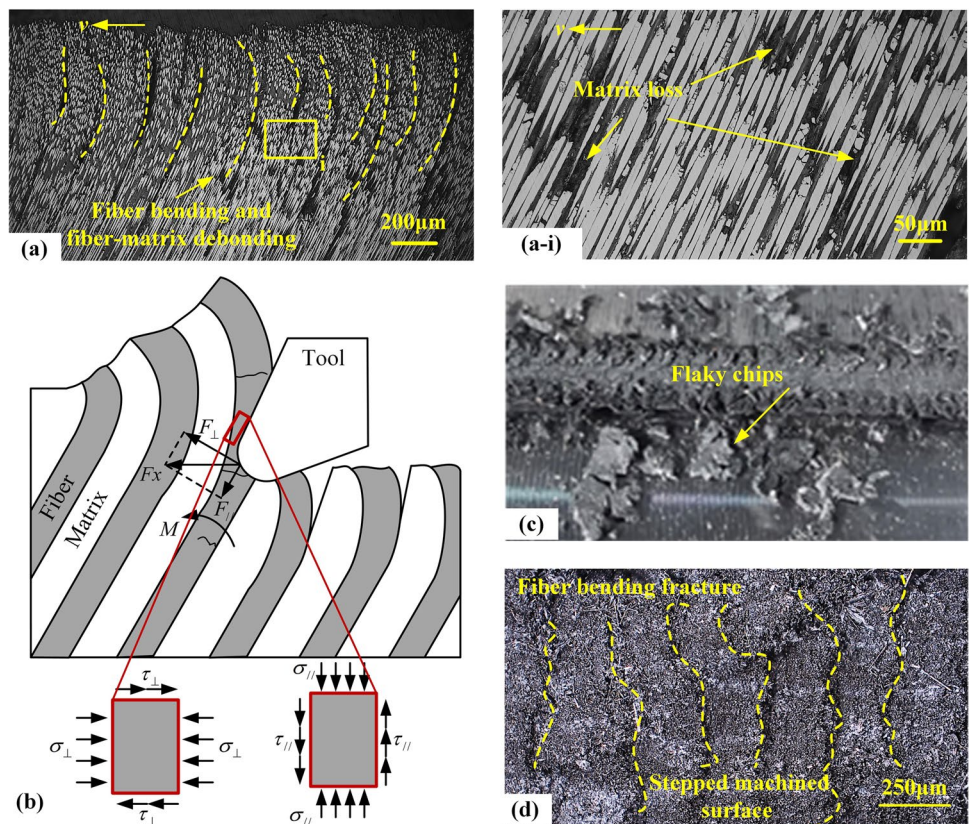
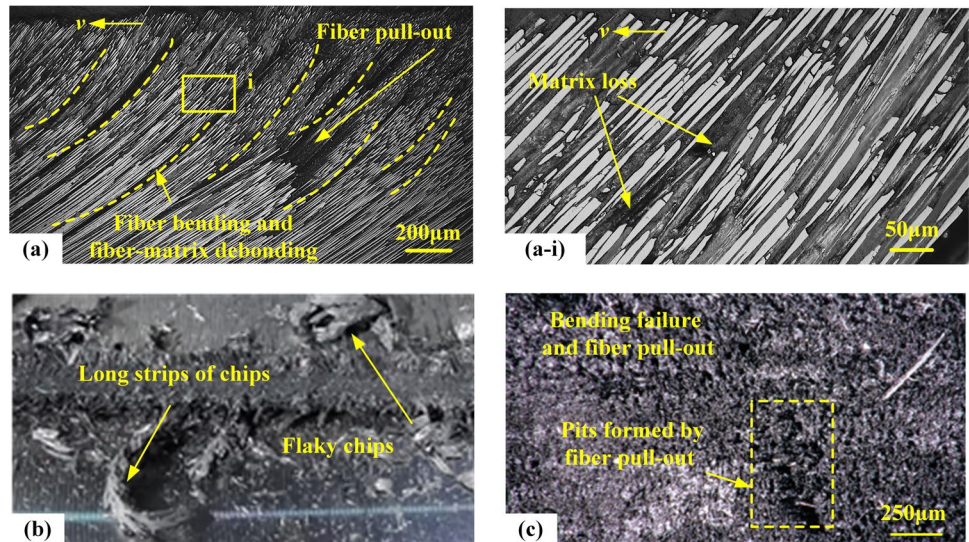


Fig. 14 At $\theta=150^\circ$: (a) the sub-surface damages of microstructure; (a-i) local enlarged detail at i in Fig. 13a; (b) the chip morphologies; (c) the micro-morphologies of machined surface



in the comparison of Fig. 7a, d and g, the depth of sub-surface damage progressively increases and the damage region formed by fiber fracture becomes larger and larger. According to Fig. 7c, f and i, the subsurface damage mode comes through the change of a large amount of matrix loss to fiber kinking. Then the position of kinking band moves down and more fibers go through large deformation, and cutting force is constantly increasing in Fig. 8c. However, the cutting force of $\theta=90^\circ$ in Fig. 8b decreases first and then increases as the cutting depth grows. Comparing with Fig. 7b, there is no obvious fiber fracture and matrix loss, but fiber bending is more obvious in Fig. 7e. While cutting depth increases to 0.06 mm in Fig. 7h, fiber kinking appears again and the fibers break at the edge of the kink band with an inclination angle of 22.5° . At the same time, the cutting force of $\theta=90^\circ$ is very high, even high up to 340 N, as shown in Fig. 8b.

(a) $v=4$ mm/s; (b) $v=7$ mm/s; (c) $v=10$ mm/s.

3.3 The cutting mechanism and chip formation

In order to reduce the damage in the process of material removal, it's necessary to figure out the cutting mechanism and chip formation of UD laminates with different fiber orientations.

In the case of $\theta=0^\circ$, the subsurface damage is shown in Fig. 9a. It can be observed that the fiber buckling and the interface debonding occur under longitudinal compression. When the edge of cutting tool contacts and squeezes the material, the fibers are compressed by the cutting force F_x along the fiber axis, producing compressive stress σ and shear stress τ as shown in Fig. 9b. The debonding appears at fiber-matrix interface induced by the shear stress τ because the compression strength of matrix is lower than that of fiber. With the movement of the tool, the fibers would be further squeezed by the rake face, bent and finally broken under compressive stress σ . The fiber and matrix flow out along the rake face of the tool, forming discontinuous and curly chips,

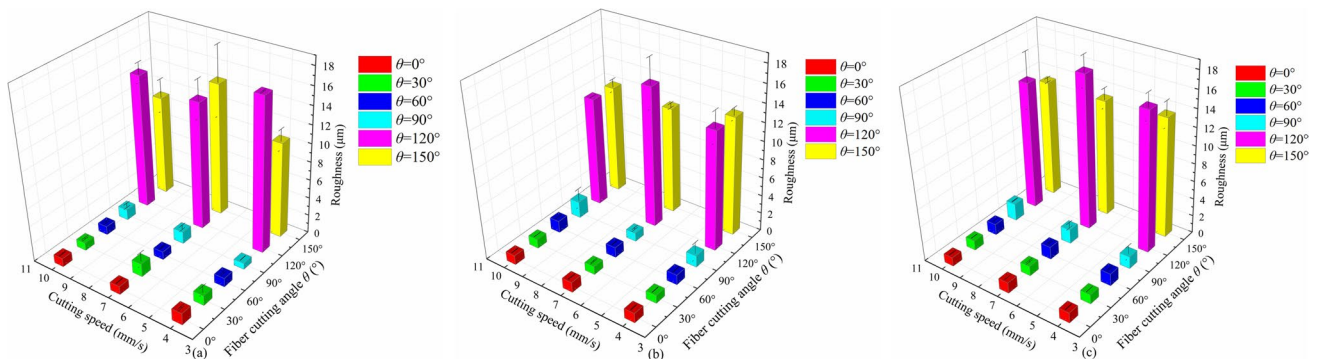
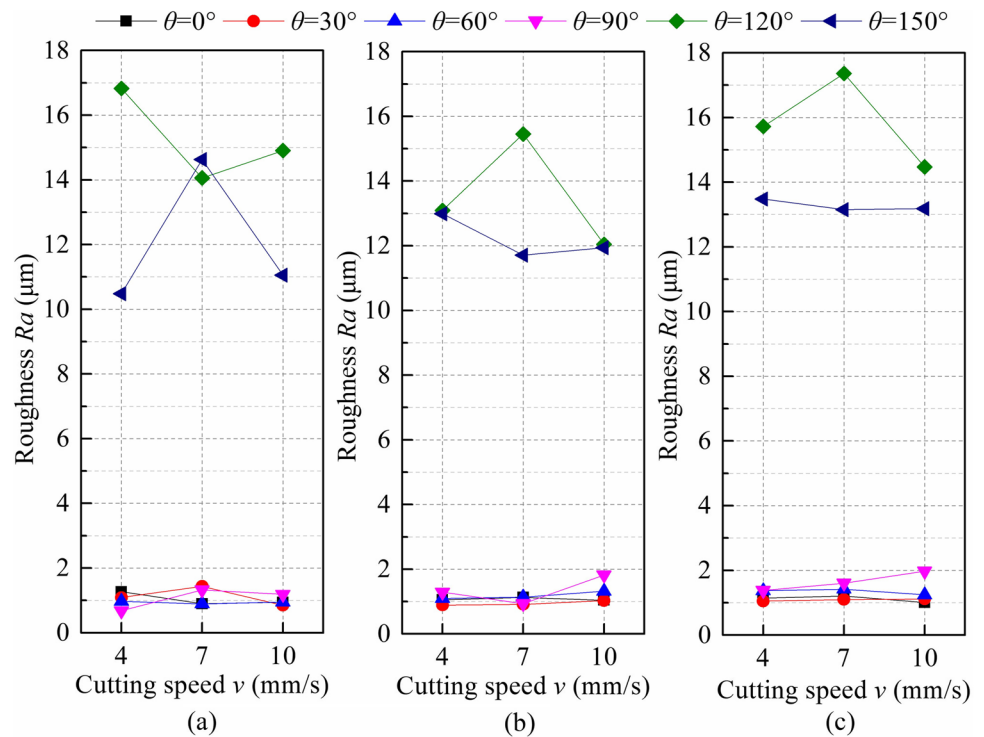


Fig. 15 The variations of machined surface roughness with fiber cutting angle at different cutting speeds and cutting depths: (a) $h=0.02$ mm; (b) $h=0.04$ mm; (c) $h=0.06$ mm

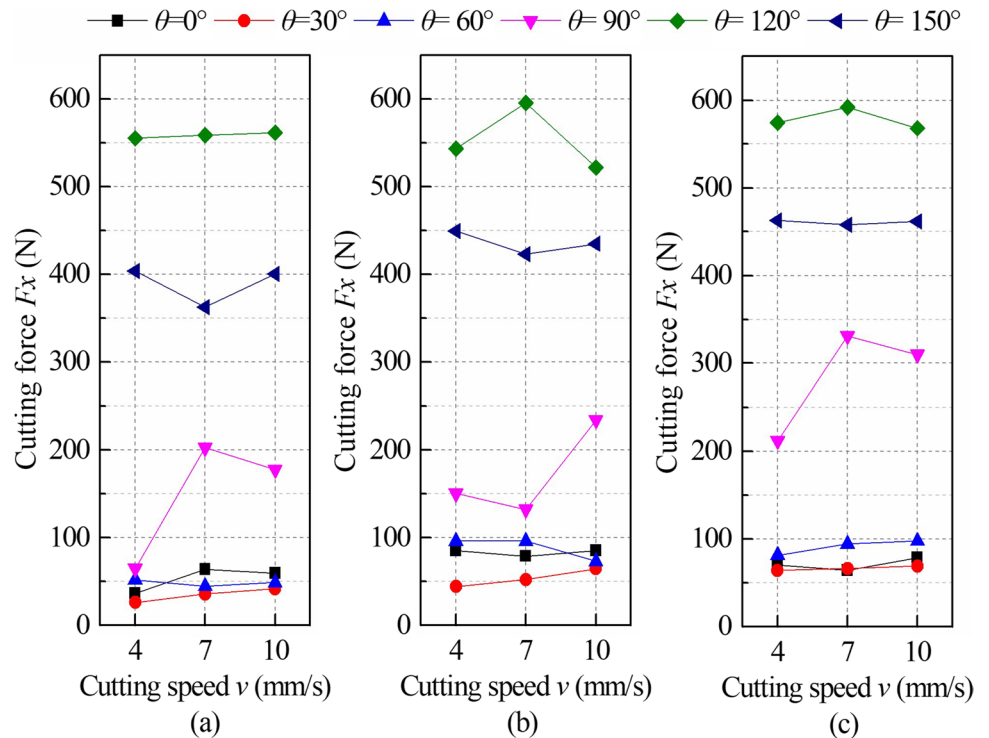
Fig. 16 The curves of machined surface roughness varying with cutting speed at different cutting depths:(a) $h=0.02$ mm; (b) $h=0.04$ mm; (c) $h=0.06$ mm



as shown in Fig. 9c. Obvious gap formed by the fiber-matrix debonding and the matrix loss were observed through the microscopic observation of the machined surface, as shown in Fig. 9d. The interface debonding is the main reason for chip formation at $\theta=0^\circ$.

At $\theta=30^\circ$, the cracks perpendicular to the fiber axial are clearly visible in Fig. 10a. At $\theta=60^\circ$, the cracks expand along the cutting direction in Fig. 11a. For $\theta < 90^\circ$, the cutting force can be decomposed into two directions: along the fiber axis and perpendicular to the fiber axis.

Fig. 17 The curves of cutting force varying with the cutting speed at three different cutting depths:(a) $h=0.02$ mm; (b) $h=0.04$ mm; (c) $h=0.06$ mm



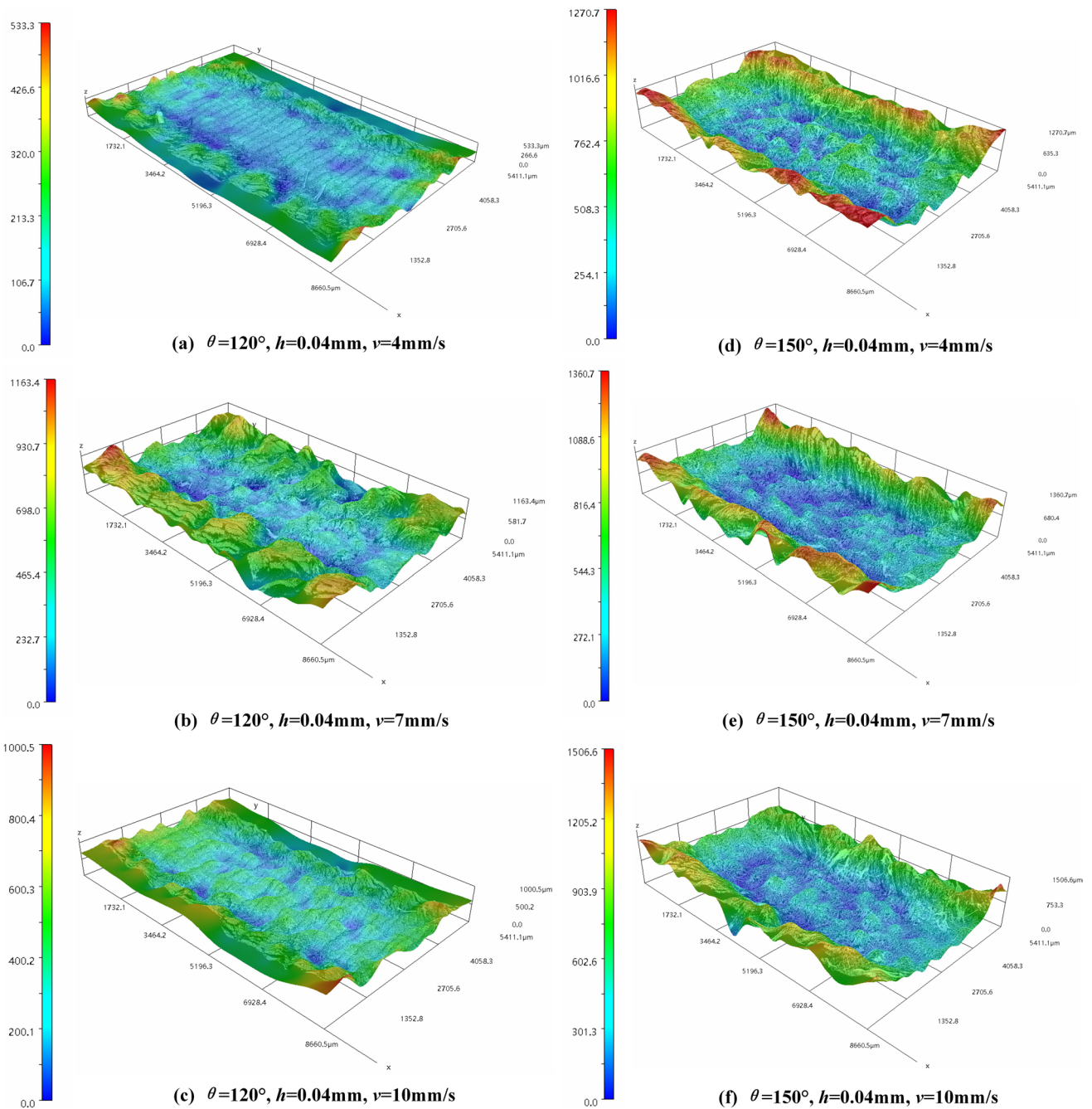


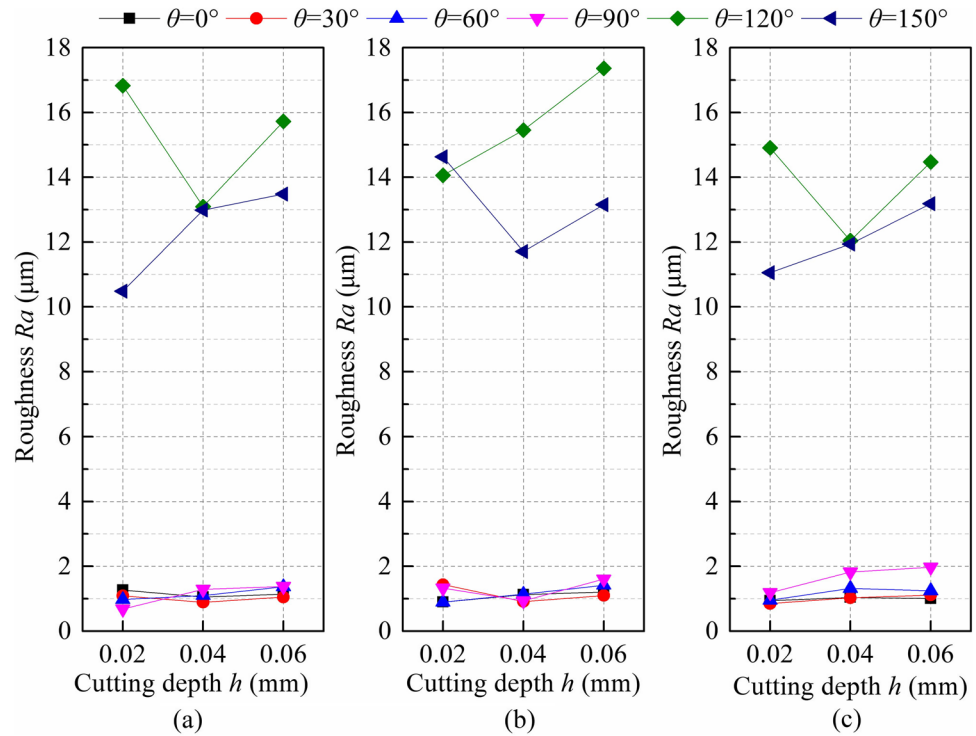
Fig. 18 The three-dimensional morphologies of machined surface: (a) $\theta=120^\circ, h=0.04\text{ mm}, v=4\text{ mm/s}$; (b) $\theta=120^\circ, h=0.04\text{ mm}, v=7\text{ mm/s}$; (c) $\theta=120^\circ, h=0.04\text{ mm}, v=10\text{ mm/s}$; (d) $\theta=150^\circ,$

$h=0.04\text{ mm}, v=4\text{ mm/s}$; (e) $\theta=150^\circ, h=0.04\text{ mm}, v=7\text{ mm/s}$; (f) $\theta=150^\circ, h=0.04\text{ mm}, v=10\text{ mm/s}$

The force perpendicular to the fiber axial compresses on the one side of fibers and forms shear stress on the cross-section of fibers, resulting in fiber-matrix debonding and fiber fracture below the machined surface, respectively. The fiber deformation and stress state are illustrated in Fig. 10b. The force along the fiber axis produces compressive stress on the cross-section of the fiber and shear stress on the lateral side of the fiber. The compressive

stress on the cross-section of the fiber further accelerates the fracture of the fiber. The shear stress on the one side of the fiber is not large enough to produce relative slippage between the fiber and matrix. The fibers are cut off by cutting edge and then slide along the rake face of the tool. Therefore, the chips shown in Fig. 10c and 11b are continuous and curly like the ductile metal materials. The quality of machined surface is excellent and only some

Fig. 19 The curves of machined surface roughness varying with cutting depth at different cutting speeds:(a) $v=4$ mm/s; (b) $v=7$ mm/s; (c) $v=10$ mm/s



holes caused by the matrix loss can be seen as shown in Fig. 10d and Fig. 11c. Besides, the white shear band formed by the fractured fibers can be clearly seen on the machined surface at $\theta=60^\circ$ in Fig. 11c, while it is not obvious at $\theta=30^\circ$ in Fig. 10d.

The irregular subsurface damage morphology of $\theta=90^\circ$ is presented in Fig. 12a. The cutting force perpendicular to the fiber axis compresses the fiber and matrix, and the uncut fibers below the machined surface are subjected to compressive stress and shear stress, as shown in Fig. 12b.

Fig. 20 The curves of cutting force varying with cutting depth at three different cutting speeds:(a) $v=4$ mm/s; (b) $v=7$ mm/s; (c) $v=10$ mm/s

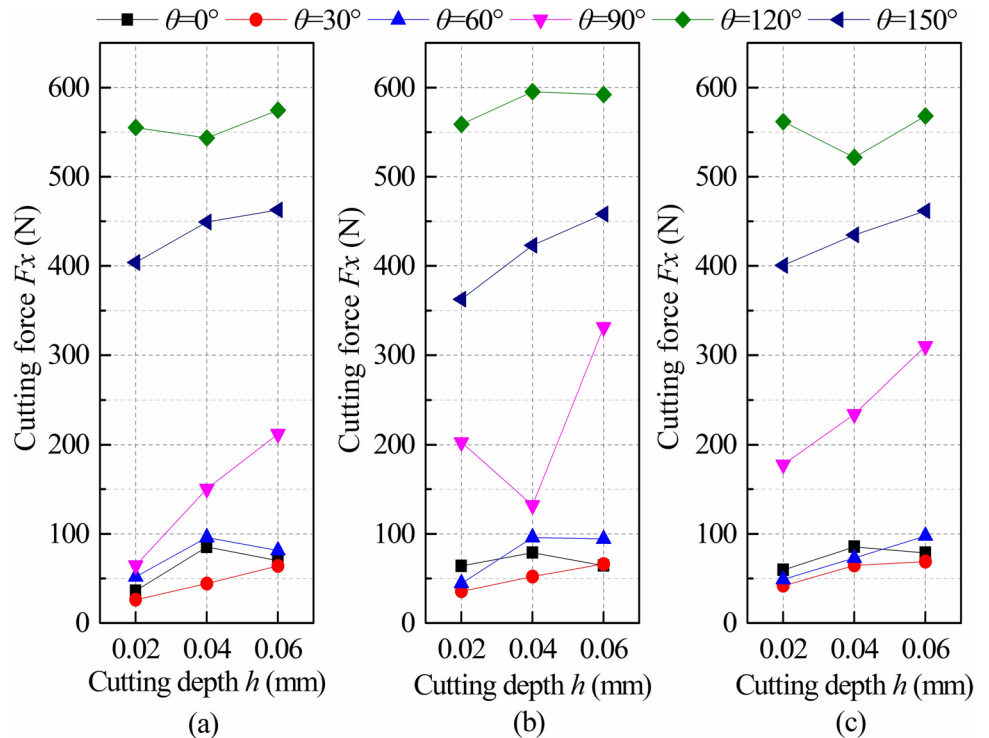


Table 3 The results of ANOVA for the machined surface roughness

Factor	DF	SS	MS	F value	P value	PD
Fiber cutting angle θ	5	3823.770	764.754	733.202	0.0001	98.60
Cutting depth h	2	8.580	4.290	4.113	0.022	0.55
Cutting speed v	2	3.807	1.904	1.825	0.171	0.25
θ^*h	10	15.825	1.583	1.517	0.159	0.20
θ^*v	10	12.183	1.218	1.168	0.332	0.16
h^*v	4	0.165	0.041	0.040	0.997	0.00
θ^*h^*v	20	36.992	1.850	1.773	0.049	0.24
Error	54	56.324	1.043			
Total	108	7035.884				

DF: Degree of freedom, SS: Sum of squares, MS: Mean squares, PD: Percentage distribution.

The fiber-matrix debonding occurs firstly, followed by fiber bending deformation. Finally, the fiber breaks under shear action resulting from cutting force F_x , leading to short flaky chips as presented in Fig. 12c. It is similar to the discontinuous cutting process of the brittle material. Chip separation is the result of the fiber-matrix debonding, fiber bending and shear fracture. The corrugated machined surface which is actually a cross section of many broken fibers at the microscopic level, is caused by different degree of elasticity recovery of deformed fiber, as seen in Fig. 12d.

In the cases of $\theta = 120^\circ$ and $\theta = 150^\circ$, the subsurface damages are shown in Fig. 13a and Fig. 14a, respectively. Fiber bending, fiber-matrix debonding and matrix loss can be observed. Both the two fiber cutting angles are greater than 105° which is the sum of the rake angle (15°) and 90° . This means that fibers contact the rake face of the tool first and then the fibers bend until they break as tool continues to feed. The compression stress σ and shear stress τ in the direction of both components are presented in Fig. 13b. Comparing Fig. 13a with Fig. 14a, the degree of fiber bending decreases but the fiber pull-out is more obvious with increase of the fiber cutting angle. This is principally because the force perpendicular to the fiber axis decreases and the force along the fiber axis increases when the fiber cutting angle ranges from 120° to 150° . The larger degree of fiber bending deformation

makes the matrix cracking intermittent. Therefore, the flaky chips come into being at $\theta = 120^\circ$ as shown in Fig. 13c and the long strips of chips are formed at $\theta = 150^\circ$ as seen in Fig. 14b. Essentially, the chip removal mechanism of both fiber cutting angles is fiber bending fracture. The position of fiber bending fracture is different in height, leading to the uneven machined surface after elasticity recovery of fibers in Fig. 13d. The periodic cracks are the result of the continuous accumulation and release of internal energy caused by fiber bending. Many pits after fiber pull-out can be seen at $\theta = 150^\circ$ in Fig. 14c.

3.4 Machined surface roughness and three-dimensional morphologies

The variations of machined surface roughness with fiber cutting angle at different cutting speeds and cutting depths are presented in Fig. 15. In the cases of $\theta \leq 90^\circ$, the fiber cutting angle has little effect on machined surface roughness. The roughness basically fluctuates around $1 \mu\text{m}$ and its maximum value does not exceed $2 \mu\text{m}$. It indicates that machined surface qualities of $\theta \leq 90^\circ$ are excellent. In the cases of $\theta = 120^\circ$ and $\theta = 150^\circ$, the machined surface roughness is significantly higher than that of $\theta \leq 90^\circ$ in Fig. 15a, b and c. This is because that there are broken fibers protruding

Table 4 Experimental results, normalized values and grey grades for the cutting force and roughness at $\theta = 120^\circ$

No	Factors			Experimental results, Y_j		Normalization, Z_j		Grey relation coefficient, ϵ_j		Grey Grade, γ	Order
	θ°	h/mm	$v/\text{mm}\cdot\text{s}^{-1}$	F_x/N	$Ra/\mu\text{m}$	F_x/N	$Ra/\mu\text{m}$	F_x/N	$Ra/\mu\text{m}$		
1	120	0.02	4	555.12	16.827	0.5460	0.1004	0.5241	0.3572	0.4407	6
2	120	0.02	7	558.83	14.059	0.4958	0.6211	0.4979	0.5689	0.5334	3
3	120	0.02	10	561.64	14.907	0.4578	0.4616	0.4797	0.4815	0.4806	5
4	120	0.04	4	543.41	13.093	0.7045	0.8029	0.6286	0.7173	0.6729	2
5	120	0.04	7	595.46	15.452	0	0.3591	0.3333	0.4383	0.3858	8
6	120	0.04	10	521.58	12.045	1	1	1	1	1	1
7	120	0.06	4	574.60	15.724	0.2823	0.3079	0.4106	0.4194	0.4150	7
8	120	0.06	7	592.08	17.361	0.0457	0	0.3438	0.3333	0.3386	9
9	120	0.06	10	568.02	14.470	0.3714	0.5438	0.4430	0.5229	0.4830	4

Table 5 Experimental results, normalized values and grey grades for the cutting force and roughness at $\theta=150^\circ$

No	Factors			Experimental results, Y_j		Normalization, Z_j		Grey relation coefficient, ϵ_j		Grey Grade, γ	Order
	$\theta/^\circ$	h/mm	$v/\text{mm}\cdot\text{s}^{-1}$	F_x/N	$Ra/\mu\text{m}$	F_x/N	$Ra/\mu\text{m}$	F_x/N	$Ra/\mu\text{m}$		
1	150	0.02	4	403.86	10.478	0.5889	1	0.5488	1	0.7744	1
2	150	0.02	7	362.73	14.629	1	0	1	0.3333	0.6667	3
3	150	0.02	10	400.58	11.055	0.6217	0.8610	0.5693	0.7825	0.6759	2
4	150	0.04	4	449.22	12.9855	0.1356	0.3959	0.3665	0.4529	0.4097	6
5	150	0.04	7	423.16	11.7065	0.3961	0.7040	0.4529	0.6282	0.5406	4
6	150	0.04	10	434.86	11.9395	0.2791	0.6479	0.4095	0.5868	0.4982	5
7	150	0.06	4	462.79	13.479	0	0.2770	0.3333	0.4089	0.3711	9
8	150	0.06	7	458.12	13.149	0.0467	0.3565	0.3440	0.4373	0.3907	7
9	150	0.06	10	461.74	13.182	0.0105	0.3486	0.3357	0.4343	0.3850	8

from the matrix, grooves formed by fiber tearing or pulling out and matrix cracks on the machined surface, which significantly increases the surface roughness at $\theta > 90^\circ$. The machined surface roughness obtains the maximum value at $\theta = 120^\circ$, indicating that machined surface quality at $\theta = 120^\circ$ is the worst. The trend of machined surface roughness is in consistent with the variation of cutting force in Fig. 4 as analyzed before. It means that the machined surface quality is related to the cutting force in general. However, it is notable that the surface roughness at $\theta = 90^\circ$ is in the same range as that in the cases of $\theta < 90^\circ$ and the cutting force of the former is obviously higher than that of the latter. That is because the cutting force is related to the subsurface damage mode such as the fiber bending deformation and fiber kinking below the machined surface. The chip removal at $\theta = 90^\circ$ is result from shear fracture of material and the cutting mechanism is not changed with cutting parameter. Therefore, the roughness of the machined surface is still low.

As for cutting speed, it is obvious that the effects of cutting speed on machined surface roughness in the cases of $\theta \leq 90^\circ$ are negligible, while the roughness at $\theta > 90^\circ$ varies significantly with increase of the cutting speed, as shown in Fig. 16. It is quite remarkable that the roughness curves of $\theta > 90^\circ$ in Fig. 16b and c show the same variation pattern at the same fiber cutting angle. With the increase of cutting speed, the roughness increases first and then decreases at $\theta = 120^\circ$. At $\theta = 150^\circ$, the roughness decreases first and then increases. The variation range of roughness at $\theta = 150^\circ$ is much smaller than that at $\theta = 120^\circ$. The above analysis shows that high cutting speed is beneficial to reduce the machined surface roughness and improve the machined surface quality, which can be attributed to the thermal softening of the matrix under high cutting temperature caused by high cutting speed, leading to reduction in cutting force. Less cutting force means low surface roughness. It can be proved by the fact that regardless of $\theta = 120^\circ$ or $\theta = 150^\circ$, the change law of surface roughness in Fig. 16b and c is the same as that of the cutting force in Fig. 17b and c respectively. The surface

roughness is related to the cutting force and the machined surface quality can also be assessed by cutting force indirectly. However, the variation trend of surface roughness with cutting speed at $\theta > 90^\circ$ in Fig. 16a are not in agreement with those in Fig. 16b and c at the same fiber cutting angle. This is because cutting depth of $h = 0.02$ mm in Fig. 16a is close to the radius of the cutting edge. The cutting depth is so small that the cutting process is unstable and the volume of cutting materials is constantly changing due to elasticity recovery of fiber below the machined surface and vibration of machining system, leading to a large displacement of the contact point between cutting edge and material. Therefore, the consistency of cutting quality is poor and the roughness variation is irregular with the increase of cutting depth.

Considering that the machined surface roughness of $\theta > 90^\circ$ varies greatly with the cutting parameters, the 3D morphologies of machined surface at $\theta = 120^\circ$ and $\theta = 150^\circ$ observed with a digital depth of field microscope are shown in Fig. 18. It is obvious that the material on both sides of the machined surface edge is higher than the machined surface. This is because the material after undergoing out-of-plane deformation at free boundary makes a concession and can't cut off by the cutting edge before its elasticity recovery. This phenomenon is similar to formation of the burrs at the exit of hole analyzed in Xu's research [41]. In the case of $\theta = 120^\circ$, the machined surface is relatively flat and shows some grooves as presented in Fig. 18a, which are derived from fiber bending fracture. With the increase of cutting speed, the machining surface is uneven, and there are pits formed by broken fibers and crushed matrix in Fig. 18b. When cutting speed further increases to $v = 10$ mm/s in Fig. 18c, the surface pits reduce and the flatness get improved but grooves occur again. It represents that fiber bending fracture is dominant, and fiber pull-out is weakened. For $\theta = 150^\circ$, it is obvious that surface evenness gradually gets better and the pits formed by pulled-out fibers reduce with increase of cutting speed as Fig. 18d, e and f. While the bare fiber bundles on both sides of the machined surface edge are more

clearly visible. It means that out-of-plane deformation and the phenomenon of material concession are more severe. It can be concluded that increasing cutting speed is helpful to improve the quality of machined surface for $\theta > 90^\circ$, as analyzed above for Fig. 16b and c.

The curves of machined surface roughness varying with cutting depth at different cutting speeds are shown in Fig. 19. It is obvious that six curves are divided into two groups, namely, $\theta > 90^\circ$ and $\theta \leq 90^\circ$. The former group process higher roughness with much larger fluctuations than latter. The grouping phenomenon indicates that the fiber cutting angle is the most essential factor affecting the roughness. The variation trend of curves at $\theta > 90^\circ$ also shows grouping phenomenon that Fig. 19a and c present the same variation tendency at the same fiber cutting angle but they are different from Fig. 19b. Also, the change laws of surface roughness in Fig. 19a and c are the same as those of the cutting force in Fig. 20a and c respectively. This proves again that there is a correlation between cutting force and surface roughness. It can be concluded that large cutting depth made the roughness high but small cutting depth cause unstable cutting process, so the medium cutting depth is recommended as optional cutting parameter. Based on the above analysis results, high cutting speed and medium cutting depth are recommended to lower cutting force and improve machined surface quality for $\theta > 90^\circ$.

3.5 Analysis of variance (ANOVA) for surface roughness and optimization of cutting parameters

Analysis of variance (ANOVA) is applied to determine which parameter significantly influences the machined surface roughness. The results of ANOVA were shown in Table 3. In ANOVA, F-value of fiber cutting angle 733.202 indicates that the fiber cutting angle is the most significant factor with the probability of < 0.0001 (“P value” less than 0.05 denote that the terms are significant). According to the results of ANOVA presented in Table 3, the most efficient factor on the roughness is found to be the fiber cutting angle as 98.60%, followed by the cutting depth (0.55%) and cutting speed (0.25%). Also, the interaction between the factors is not significant.

In order to determine the optimal cutting parameters for $\theta > 90^\circ$, the cutting force and machined surface roughness were simultaneously optimized with grey relational analysis (GRA). The cutting parameters are optimized through the following steps:

- 1) The reference data that reflect the characteristics of the system behavior and the comparative data that affect the system behavior are determined.
- 2) The variables are converted into proper dimensionless indexes.

- 3) The grey relational coefficient and grey relational grade are calculated.
- 4) The grey relational grade is ranked and the optimal parameters are selected.

According to Analysis of variance (ANOVA) above, the fiber cutting angle is the most significant factor accounting for 98.60%. Therefore, the optimal cutting parameters at $\theta = 120^\circ$ and $\theta = 150^\circ$ were analyzed respectively. For $\theta = 120^\circ$, experimental results for the cutting force and roughness are given in Table 4. For calculating the grey grade, the cutting force and roughness are normalized according to the following expression.

$$Z_j(k) = \frac{\max_j[Y_j(k)] - Y_j(k)}{\max_j[Y_j(k)] - \min_j[Y_j(k)]} \tag{1}$$

where $Y_j(k)$ is the original value to be normalized, $\max_j[Y_j(k)]$ is the largest value of $Y_j(k)$, and $\min_j[Y_j(k)]$ is the smallest value of $Y_j(k)$.

For example, the normalized value for $j = 1 - 2, k = 1 - 9$ can be computed as follows.

$$Y_1(1) = (595.46 - 555.12)/(595.46 - 521.58) = 0.546020574 \tag{2}$$

$$Y_2(1) = (17.3605 - 14.059)/(17.3605 - 12.045) = 0.100366852 \tag{3}$$

Grey relational coefficient $\epsilon_j(k)$ is calculated to express the relationship between the ideal and actual normalized experimental results. The grey relational coefficient $\epsilon_j(k)$ can be expressed as follows.

$$\epsilon_j(k) = \frac{\left\{ \min_j \min_k |Z_j(k) - Z_0(j)| + \xi \max_j \max_k |Z_j(k) - Z_0(j)| \right\}}{\left\{ |Z_j(k) - Z_0(j)| + \xi \max_j \max_k |Z_j(k) - Z_0(j)| \right\}} \tag{4}$$

where $Z_0(j)$ is the ideal sequence which has the value of 1, and $\epsilon_j(k)$ is the grey relational coefficient of the j -th performance characteristic of the k -th experiment. Distinguishing coefficient ξ is defined in the range of $0 \leq \xi \leq 1$. It is generally taken as 0.5.

For example, the grey relational coefficient for $j = 1 - 2, k = 1 - 9$ can be computed as follows.

$$\epsilon_1(1) = (0 + 0.5 \times 1) / (0.546020574 - 1 + 0.5 \times 1) = \frac{0.5}{1.5 - 0.546020574} = 0.524120318 \tag{5}$$

$$\epsilon_2(1) = (0 + 0.5 \times 1) / (0.100366852 - 1 + 0.5 \times 1) = \frac{0.5}{1.5 - 0.100366852} = 0.357236466 \tag{6}$$

Grey relational grade γ_k for the k -th experiment can be determined from the following equation.

$$\gamma_k = \frac{1}{n} \sum_{j=1}^n \varepsilon_j(k) \quad (7)$$

where n is the number of responses. For example, the grey relational grade for cutting force at test 1 can be calculated as follow.

$$\gamma_1 = \frac{1}{2}(0.524120318 + 0.357236466) = 0.4406784 \quad (8)$$

The calculated grey relational grades for each test were put in order from maximum (optimum) to minimum and then they were presented in the Table 4. The optimal value, which was the maximum of grey relational grade, was found to be the 6th experiment for initial parameters. The minimum of the cutting force and machined surface roughness can be simultaneously obtained at the optimal machining conditions, which is $h=0.04$ mm and $v=10$ mm/s for $\theta=120^\circ$. For $\theta=150^\circ$, the optimal machining conditions are $h=0.02$ mm and $v=4$ mm/s, as shown in Table 5.

4 Conclusions

Investigations on chip formation mechanism and influencing rule of various factors in orthogonal cutting of UD laminates was conducted. The cutting force, thrust force, cutting mechanism, chip formation, machined surface roughness and three-dimensional morphologies were analyzed, especially the effect of the fiber cutting angle, cutting speed and cutting depth. The conclusions can be drawn as follows:

(1) The cutting forces of $\theta > 90^\circ$ are 7.58 times higher than those of $\theta < 90^\circ$. Both cutting speed and cutting depth have the greatest influence on the cutting force at $\theta = 90^\circ$, and the effect of cutting depth on the cutting force is more significant than that of cutting speed. The thrust force increases with the growth of the fiber cutting angle and reaches the maximum value at $\theta = 90^\circ$. In the cases of $\theta > 90^\circ$, the thrust force switches to negative value, which means that the force produced by cutting material with a tool in the vertical direction changes from downward push to upward pull. It's due to the elasticity recovery of the deformed fiber. Thrust force still increases with fiber cutting angle in the opposite direction.

(2) The micromorphology of machined surface and subsurface revealed four typical cutting mechanisms, namely, interface-debonding, fracture-sliding, shearing-fracture, and bending-fracture in the range of $\theta = 0 \sim 180^\circ$. Four corresponding chip patterns are also presented, namely, discontinuous and curly chips, continuous and curly chips, short flaky chips and flaky or long curly chips. The cutting parameters have the greatest effect on subsurface damage at $\theta = 90^\circ$. The degree of fiber bending deformation and

the characteristics of fiber kinking change constantly with variation of cutting speed and cutting depth.

(3) The variation of roughness with cutting depth or cutting speed shows grouping phenomenon that roughness fluctuates around $1 \mu\text{m}$ at $\theta \leq 90^\circ$ while it is more than $11 \mu\text{m}$ and up to $15 \mu\text{m}$ at $\theta > 90^\circ$. In the latter cases, the effect of cutting parameters on roughness is obvious and the variation of surface roughness with cutting parameters is in consistent with that of cutting force. The chip removal at $\theta = 90^\circ$ is result from shear fracture of material and the cutting mechanism is not changed with cutting parameter. Therefore, the roughness of the machined surface at $\theta = 90^\circ$ is in the same range as $\theta < 90^\circ$ and is at a low level.

(4) The most efficient factor on the roughness is found to be the fiber cutting angle accounting for 98.60%, followed by the cutting depth (0.55%) and cutting speed (0.25%). The interaction between the factors is not significant by ANOVA. According to the results of GRA, the minimum of the cutting force and machined surface roughness can be simultaneously obtained at $h=0.04$ mm and $v=10$ mm/s for $\theta=120^\circ$. For $\theta=150^\circ$, the optimal machining conditions are $h=0.02$ mm and $v=4$ mm/s.

The results of this paper would help further promote the application of CFRP in industries such as aerospace and defense.

(1) The further direction of this research is to evaluate the macroscopic machining damage in drilling or milling of CFRP, establish the correlation model of macro and micro cutting parameters to provide theoretical basis for control of macro parameter and finally combine the results with intelligent technology to realize the dynamic monitoring and control of machining quality in the actual manufacturing process in real-time.

(2) In order to improve the machining quality and reduce the experimental cost, mechanical theoretical model and finite element model can be used to predict cutting force and damage state based on cutting mechanism and micro-damage evolution of CFRP. A new processing strategy with variable cutting parameters and innovative cutting tool are urgently developed to improve traditional process in the future.

Author Contributions All authors contributed to the study conception and design. Material preparation was performed by Shengping Zhang and Junshan Hu. Test execution and data collection were completed by Shengping Zhang, Ruihao Kang and Jiali Yu. Data analysis was conducted by Shengping Zhang, Junshan Hu, Shanyong Xuan and Wei Tian. The first draft of the manuscript was written by Shengping Zhang and all authors commented on previous versions of the manuscript. All authors read and approved the final manuscript.

Funding This work is financially supported by National Natural Science Foundation of China (Grant No. 52005259), China Postdoctoral Science Foundation (Grant No. 2022M720939), Anhui Provincial Key Research and Development Plan (Grant No. 202203a05020039) and Jiangsu Key Laboratory of Precision and Micro-Manufacturing Technology Foundation (Grant No. ZAA20003-05). Moreover, the authors

would like to acknowledge the editors and the anonymous referees for their insightful comments.

Data Availability The raw/processed data required to reproduce these findings cannot be shared at this time as the data also forms part of an ongoing study.

Declarations

Ethics approval Not applicable.

Informed consent Additional informed consent was obtained from all individual participants for whom identifying information is included in this paper.

Competing Interests The authors declared that they have no conflicts of interest to this work.

References

- Che DM, Saxena I, Han PD, Guo P, Ehmann KF (2014) Machining of Carbon Fiber Reinforced Plastics/Polymers: A Literature Review. *J Manuf Sci E-T Asme* 136(3):034001. <https://doi.org/10.1115/1.4026526>
- Dandekar CR, Shin YC (2012) Modeling of machining of composite materials: A review. *Int J Mach Tool Manu* 57:102–121. <https://doi.org/10.1016/j.ijmactools.2012.01.006>
- Geier N, Davim JP, Szalay T (2019) Advanced cutting tools and technologies for drilling carbon fibre reinforced polymer (CFRP) composites: A review. *Compos Part a-Appl S* 125:105552. <https://doi.org/10.1016/j.compositesa.2019.105552>
- Arola D, Ramulu M (1997) Net shape manufacturing and the performance of polymer composites under dynamic loads. *Exp Mech* 37(4):379–385. <https://doi.org/10.1007/Bf02317300>
- Turki Y, Habak M, Velasco R, Aboura Z, Khellil K, Vantomme P (2014) Experimental investigation of drilling damage and stitching effects on the mechanical behavior of carbon/epoxy composites. *Int J Mach Tool Manu* 87:61–72. <https://doi.org/10.1016/j.ijmactools.2014.06.004>
- Khashaba UA (2013) Drilling of polymer matrix composites: A review. *J Compos Mater* 47(15):1817–1832. <https://doi.org/10.1177/0021998312451609>
- Singh AP, Sharma M, Singh I (2013) A review of modeling and control during drilling of fiber reinforced plastic composites. *Compos Part B-Eng* 47:118–125. <https://doi.org/10.1016/j.compositesb.2012.10.038>
- Ghidossi P, El Mansori M, Pierron F (2006) Influence of specimen preparation by machining on the failure of polymer matrix off-axis tensile coupons. *Compos Sci Technol* 66(11–12):1857–1872. <https://doi.org/10.1016/j.compscitech.2005.10.009>
- Hintze W, Hartmann D, Schutte C (2011) Occurrence and propagation of delamination during the machining of carbon fibre reinforced plastics (CFRPs) - An experimental study. *Compos Sci Technol* 71(15):1719–1726. <https://doi.org/10.1016/j.compscitech.2011.08.002>
- Jung JP, Kim GW, Lee KY (2005) Critical thrust force at delamination propagation during drilling of angle-ply laminates. *Compos Struct* 68(4):391–397. <https://doi.org/10.1016/j.compstruct.2004.04.004>
- Karpat Y, Bahtiyar O, Deger B (2012) Mechanistic force modeling for milling of unidirectional carbon fiber reinforced polymer laminates. *Int J Mach Tool Manu* 56:79–93. <https://doi.org/10.1016/j.ijmactools.2012.01.001>
- Killickap E (2010) Optimization of cutting parameters on delamination based on Taguchi method during drilling of GFRP composite. *Expert Syst Appl* 37(8):6116–6122. <https://doi.org/10.1016/j.eswa.2010.02.023>
- Enemuoh EU, El-Gizawy AS, Okafor AC (2001) An approach for development of damage-free drilling of carbon fiber reinforced thermosets. *Int J Mach Tool Manu* 41(12):1795–1814. [https://doi.org/10.1016/S0890-6955\(01\)00035-9](https://doi.org/10.1016/S0890-6955(01)00035-9)
- Phadnis VA, Makhadmeh F, Roy A, Silberschmidt VV (2013) Drilling in carbon/epoxy composites: Experimental investigations and finite element implementation. *Compos Part a-Appl S* 47:41–51. <https://doi.org/10.1016/j.compositesa.2012.11.020>
- Shyha I, Soo SL, Aspinwall D, Bradley S (2010) Effect of laminate configuration and feed rate on cutting performance when drilling holes in carbon fibre reinforced plastic composites. *J Mater Process Tech* 210(8):1023–1034. <https://doi.org/10.1016/j.jmatprotec.2010.02.011>
- Wen Q, Guo DM, Gao H, Wang B (2014) Burr and spalling damages formation mechanism of carbon/epoxy composites by scratching experiment. *Acta Mater Compos Sin* 31(1):9–17. <https://doi.org/10.13801/j.cnki.fhclxb.2014.01.005>
- Azmi AI, Lin RJT, Bhattacharyya D (2013) Machinability study of glass fibre-reinforced polymer composites during end milling. *Int J Adv Manuf Tech* 64(1–4):247–261. <https://doi.org/10.1007/s00170-012-4006-6>
- Ucar M, Wang Y (2005) End-milling machinability of a carbon fiber reinforced laminated composite. *J Adv Mater-Covina* 37(4):46–52
- Wang FJ, Wang D, Yin JW, Yang F (2019) Analysis of Surface Damage Formation Mechanism in Milling of CFRPs. *J Mech Eng* 55(13):195–204. <https://doi.org/10.3901/JME.2019.13.195>
- Yashiro T, Ogawa T, Sasahara H (2013) Temperature measurement of cutting tool and machined surface layer in milling of CFRP. *Int J Mach Tool Manu* 70:63–69. <https://doi.org/10.1016/j.ijmactools.2013.03.009>
- Koplev A (1980) Cutting of CFRP with Single Edge Tools. *Proceedings of the Third International Conference on Composite Materials* 1597–1605 <https://doi.org/10.1016/B978-1-4832-8370-8.50126-1>
- Cheng H, Gao JY, Kafka OL, Zhang KF, Luo B, Liu WK (2017) A micro-scale cutting model for UD CFRP composites with thermo-mechanical coupling. *Compos Sci Technol* 153:18–31. <https://doi.org/10.1016/j.compscitech.2017.09.028>
- Chen R, Li SJ, Li PN, Liu XP, Qiu XY, Ko TJ, Jiang Y (2020) Effect of fiber orientation angles on the material removal behavior of CFRP during cutting process by multi-scale characterization. *Int J Adv Manuf Tech* 106(11–12):5017–5031. <https://doi.org/10.1007/s00170-020-04968-w>
- Wang XM, Zhang LC (2003) An experimental investigation into the orthogonal cutting of unidirectional fibre reinforced plastics. *Int J Mach Tool Manu* 43(10):1015–1022. [https://doi.org/10.1016/S0890-6955\(03\)00090-7](https://doi.org/10.1016/S0890-6955(03)00090-7)
- Jahromi AS, Bahr B, Krishnan KK (2014) An analytical method for predicting damage zone in orthogonal machining of unidirectional composites. *J Compos Mater* 48(27):3355–3365. <https://doi.org/10.1177/0021998313509862>
- Rentsch R (2013) Crack Formation and Crack Path in CFRP Machining. *International Conference on Crack Path*
- Bhatnagar N, Ramakrishnan N, Naik NK, Komanduri R (1995) On the Machining of Fiber-Reinforced Plastic (Frp) Composite Laminates. *Int J Mach Tool Manu* 35(5):701–716. [https://doi.org/10.1016/0890-6955\(95\)93039-9](https://doi.org/10.1016/0890-6955(95)93039-9)
- Agarwal H, Amaranath A, Jamthe Y, Gururaja S (2015) An investigation of cutting mechanisms and strain fields during orthogonal cutting in CFRPs. *Mach Sci Technol* 19(3):416–439. <https://doi.org/10.1080/10910344.2015.1051539>
- An QL, Cai CY, Cai XJ, Chen M (2019) Experimental investigation on the cutting mechanism and surface generation in orthogonal cutting of UD-CFRP laminates. *Compos Struct* 230:111441. <https://doi.org/10.1016/j.compstruct.2019.111441>

30. Rao GVG, Mahajan P, Bhatnagar N (2007) Micro-mechanical modeling of machining of FRP composites - Cutting force analysis. *Compos Sci Technol* 67(3–4):579–593. <https://doi.org/10.1016/j.compscitech.2006.08.010>
31. Rao GVG, Mahajan P, Bhatnagar N (2008) Three-dimensional macro-mechanical finite element model for machining of unidirectional-fiber reinforced polymer composites. *Mat Sci Eng a-Struct* 498(1–2):142–149. <https://doi.org/10.1016/j.msea.2007.11.157>
32. Hassouna A, Mzali S, Zemzemi F, Mezlini S (2020) Orthogonal cutting of UD-CFRP using multiscale analysis: Finite element modeling. *J Compos Mater* 54(18):2505–2518. <https://doi.org/10.1177/0021998319899129>
33. Yan XY, Reiner J, Bacca M, Altintas Y, Vaziri R (2019) A study of energy dissipating mechanisms in orthogonal cutting of UD-CFRP composites. *Compos Struct* 220:460–472. <https://doi.org/10.1016/j.compstruct.2019.03.090>
34. Zenia S, Ben Ayed L, Nouari M, Delameziere A (2015) Numerical prediction of the chip formation process and induced damage during the machining of carbon/epoxy composites. *Int J Mech Sci* 90:89–101. <https://doi.org/10.1016/j.ijmecsci.2014.10.018>
35. Lasri L, Nouari M, El Mansori M (2009) Modelling of chip separation in machining unidirectional FRP composites by stiffness degradation concept. *Compos Sci Technol* 69(5):684–692. <https://doi.org/10.1016/j.compscitech.2009.01.004>
36. Mahdi M, Zhang LC (2001) A finite element model for the orthogonal cutting of fiber-reinforced composite materials. *J Mater Process Tech* 113(1–3):373–377. [https://doi.org/10.1016/S0924-0136\(01\)00675-6](https://doi.org/10.1016/S0924-0136(01)00675-6)
37. Abena A, Soo SL, Essa K (2017) Modelling the orthogonal cutting of UD-CFRP composites: Development of a novel cohesive zone model. *Compos Struct* 168:65–83. <https://doi.org/10.1016/j.compstruct.2017.02.030>
38. Soldani X, Santiuste C, Munoz-Sanchez A, Miguelez MH (2011) Influence of tool geometry and numerical parameters when modeling orthogonal cutting of LFRP composites. *Compos Part a-Appl S* 42(9):1205–1216. <https://doi.org/10.1016/j.compositesa.2011.04.023>
39. Langella A, Nele L, Maio A (2005) A torque and thrust prediction model for drilling of composite materials[J]. *Compos Part A Appl Sci Manuf* 36(1):83–93. <https://doi.org/10.1016/j.compositesa.2004.06.024>
40. Miah F, De-Luycker E, Lachaud F, Landon Y, Piquet R (2019) Effect of Different Cutting Depths to the Cutting Forces and Machining Quality of Cfrp Parts in Orthogonal Cutting - a Numerical and Experimental Comparison. *Proceedings of the Asme International Mechanical Engineering Congress and Exposition, 2018, Vol 1*
41. Xu JY, An QL, Cai XJ, Chen M (2013) Drilling machinability evaluation on new developed high-strength T800S/250F CFRP laminates. *Int J Precis Eng Man* 14(10):1687–1696. <https://doi.org/10.1007/s12541-013-0252-2>

Publisher's note Springer Nature remains neutral with regard to jurisdictional claims in published maps and institutional affiliations.

Springer Nature or its licensor (e.g. a society or other partner) holds exclusive rights to this article under a publishing agreement with the author(s) or other rightsholder(s); author self-archiving of the accepted manuscript version of this article is solely governed by the terms of such publishing agreement and applicable law.